A Computational Model of Bidirectional Axonal Growth in Micro-Tissue Engineered Neuronal Networks (micro-TENNs)

Toma Marinov[1], Liang Yuchi[1], Dayo O. Adewole[3, 4, 5], D. Kacy Cullen[3, 4, 5], Reuben H. Kraft[1, 2]

[1] Penn State Computational Biomechanics Group, Mechanical and Nuclear Engineering, Pennsylvania State University, University Park, PA, USA, [2] Department of Biomedical Engineering, Pennsylvania State University, University Park, PA, USA, [3] Center for Brain Injury & Repair, Department of Neurosurgery, Perelman School of Medicine, University of Pennsylvania, Philadelphia, PA, USA, [4] Department of Bioengineering, School of Engineering & Applied Science, University of Pennsylvania, Philadelphia, PA, USA, [5] Center for Neurotrauma, Neurodegeneration & Restoration, Corporal Michael J. Crescenz Veterans Affairs Medical Center, Philadelphia, PA, USA.

Abstract

Micro-Tissue Engineered Neural Networks (Micro-TENNs) are living three-dimensional constructs designed to replicate the neuroanatomy of white matter pathways in the brain, and are being developed as implantable microtissue for axon tract reconstruction or as anatomically-relevant *in vitro* experimental platforms. Micro-TENNs are composed of discrete neuronal aggregates connected by bundles of long-projecting axonal tracts within miniature tubular hydrogels. In order to help design and optimize micro-TENN performance, we have created a new computational model including geometric and functional properties. The model is built upon the three-dimensional diffusion equation and incorporates large-scale uni- and bi-directional growth that simulates realistic neuron morphologies. The model captures unique features of 3D axonal tract development that are not apparent in planar outgrowth, and may be insightful for how white matter pathways form during brain development. The processes of axonal outgrowth, branching, turning and aggregation/bundling from each neuron are described through functions built on concentration equations and growth time distributed across the growth segments. Once developed we conducted multiple parametric studies to explore the applicability of the method and conducted preliminary validation via comparisons to experimentally grown micro-TENNs for a range of growth conditions. Using this framework, this model can be applied to study micro-TENN growth processes and functional characteristics using spiking network or compartmental network modeling. This model may be applied to improve our understanding of axonal tract development and functionality, as well as to optimize the fabrication of implantable tissue engineered brain pathways for nervous system reconstruction and/or modulation.

Introduction

Various neural tissue engineering tools have been created to model and study the development of neuronal networks *in vitro*. Among them are micro-tissue engineered neural networks (micro-TENNs), which are three-dimensional (3D) living constructs comprised of long-projecting axonal

1

39 tracts and discrete neuronal populations within a microscopic, hollow hydrogel cylinder
40 (microcolumn) filled with an extracellular matrix (ECM) [1]. Preformed clusters of neuronal cell
41 bodies (aggregates) are housed at one or both ends of the microcolumn, with axons growing
42 longitudinally through the hydrogel lumen (**Figure 1**). This segregation of long axonal tracts and
43 neuronal cell bodies approximates the network architecture of the central nervous system by
44 replicating the anatomy of gray matter and white matter pathways referred to as the
45 "connectome". Micro-TENNs may be fabricated with a range of neuronal subtypes and physical
46 properties, yielding a controllable yet biofidelic microenvironment for studying 3D neural
47 networks *in vitro*. As such, micro-TENNs are being developed in parallel as (1) self-contained,
48 bioengineered implants to reconstruct compromised pathways in the brain, and (2) biofidelic
49 test-beds for studying various neuronal phenomena (e.g. growth, synaptic integration, circuit
50 development, pathological responses) [1]–[5]. Towards the former, prior work has shown that
51 micro-TENNs are capable of survival, maintenance of architecture, neurite outgrowth, and
52 host/implant synaptic integration out to at least 1 month following implant in adult rats [3]–[6].

53
54 To advance micro-TENNs' capabilities as an *in vitro* test-bed and/or to rebuild the damaged
55 connectome, one of our design goals is to develop a computational platform that can be used to
56 design and optimize micro-TENNs for specific performance goals. To be able to investigate
57 neuronal growth, neurite extension, and the formation of synaptic connectivity at the distal ends,
58 we need a simulation framework that can generate large-scale unidirectional and bidirectional
59 axonal outgrowth with realistic neuron morphologies. The applications of this computational
60 framework in micro-TENNs include: (i) study processes involved in outgrowth and structural
61 integration in 3D microenvironments; (ii) aid in the design and optimization of functional
62 characteristics and predict performance (e.g., output for a given input); (iii) simulate detailed
63 neuron morphologies and anatomically-relevant neuronal-axonal networks to study
64 connectome-level functional connectivity via spiking or compartmental network modeling.
65 Combining the anatomical simulation results and the study of functional connectivity will
66 increase our ability to understand and predict the neurophysiological characteristics and
67 network-level activity in the micro-TENNs.
68
69 There are two major approaches to simulate neuronal development: construction algorithms and
70 biologically-inspired growth processes [7]. Construction algorithms aim to reproduce the shape
71 of real dendritic trees from distributions of shape parameters [8], [9]. However, this approach
72 lacks the insight into any underlying biophysical mechanisms, such as the influences on
73 morphological development caused by different neuronal types [10], a neuron's intracellular
74 environment and interaction with other neurons. Stochastic growth models, which provide a
75 description of the growth process based on probabilistic growing events [11]–[14], is a popular
76 approach under construction algorithms. Biologically-inspired growth processes are based on a
77 description of the underlying biophysical mechanisms of the dendritic development [10], [15],
78 [16]. The studies were conducted within various aspects of development, such as cell migration
79 [17], neurite extension [18], growth cone steering [19], [20] and synapse formation [21].
80
81
82 In this paper, we present an ad-hoc growth model built upon the diffusion principle, which
83 incorporates the stochastic process to reproduce the shape of micro-TENNs tissue. In that
84 sense it belongs to the construction algorithms, however it does not rely on experimentally
85 determined shape parameters. Our approach uses the 3D diffusion equation imposed with
86 various rules for individual neuronal growth, such as the actions of neurite extension, branching,

87   turning and aggregation/bundling. The concentration gradients guide the development of the
88   axonal and dendritic neurites and describe the competition for resources between different
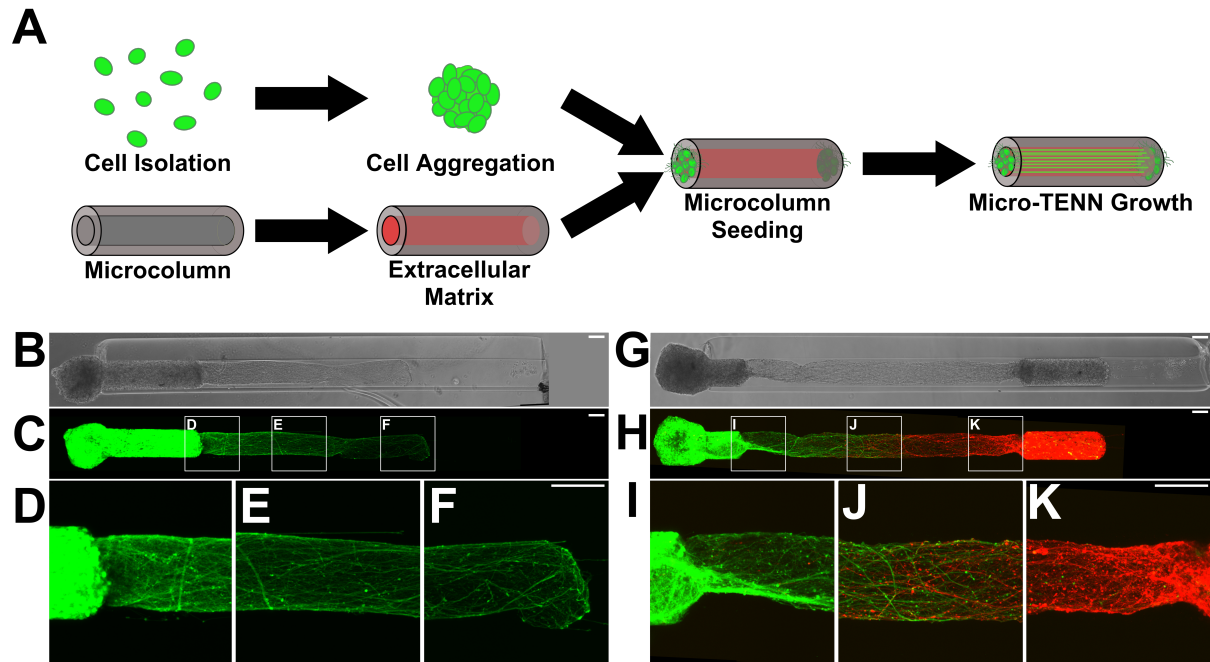89   growth tips of individual dendrites or axons.

90

Figure 1. Micro-TENNs as living, 3D neuronal-axonal constructs. (A) Micro-TENNs are fabricated in a three-step process. Neurons are isolated and forced into spherical aggregates via gentle centrifugation (top). Simultaneously, single-channel microcolumns are cast from hydrogel to a predetermined inner and outer diameter and filled with an extracellular matrix (ECM) comprised of collagen and laminin (bottom). Next, ECM-filled microcolumns are seeded with either 1 aggregate or 2 aggregates to form either unidirectional or bidirectional micro-TENNs, respectively. Micro-TENNs are then grown *in vitro*. **(B)** Phase microscopy image of a unidirectional, GFP-positive micro-TENN at 5 days in vitro (DIV). **(C-F)** Confocal micrograph of same micro-TENN from (B). Axons can be seen projecting from the neuronal aggregate **(D)** and extending through the ECM-filled microcolumn **(E, F)**. **(G)** Phase micrograph of a bidirectional micro-TENN at 5 DIV. The two aggregates have been individually transduced to express GFP (left) and mCherry (right), allowing for identification and monitoring of aggregate-specific processes. **(H-K)** Confocal micrograph of the micro-TENN from **(G)**, showing axons projecting from each aggregate **(I, K)** and growing along each other **(J)**. Scale bars: 100 µm.

91

Methods

Micro-TENN Fabrication and Experimental Measurements

94   Micro-TENNs were generated as previously described [4]. Briefly, agarose (3% w/v) was cast in
95   a custom-designed acrylic mold to yield microcolumns with an outer diameter of 345 or 398 µm
96   and inner diameter of 180 µm. Microcolumns were UV-sterilized and cut to a specified length
97   before the lumen was filled with an ECM comprised of rat tail collagen 1 (1 mg/mL) and mouse
98   laminin (1 mg/mL) adjusted to a pH of 7.2-7.4 (Reagent Proteins, San Diego, CA). To create the
99   neuronal aggregates, embryonic day 18 (E18) cortical neurons were isolated from rodents and
100 dissociated. The resultant single-cell suspensions were added to custom PDMS pyramidal wells
101 and centrifuged at 200 x *g* for 5 minutes to force the cells into spheroidal aggregates. Following

3

102 24h incubation at 37˚C/5% CO_2, aggregates were seeded within the microcolumns to generate
103 unidirectional (with one aggregate) and bidirectional (with one aggregate at each end) micro-
104 TENNs. Micro-TENNs were then grown at 37˚C/5% CO_2 with half-media changes every 48
105 hours. To fluorescently label aggregates, adeno-associated virus 1 (AAV1) was sourced from
106 the Penn Vector Core (Philadelphia, PA), packaged with the human synapsin 1 promoter and
107 either green fluorescent protein (GFP) or the red fluorescent protein mCherry, and added to the
108 pyramidal wells containing the aggregates (final titer: $\sim 3 \times 10^{10}$). Aggregates were kept at 37˚C,
109 5% CO_2 overnight before being seeded in micro-columns as described.

110 During the design and early development of the model, unidirectional and bidirectional micro-
111 TENNs were generated with approximately 15-30E^3 neurons per aggregate and lengths ranging
112 from 2.0-9.0mm (n = 39), with growth rates analyzed as described [5]. To identify aggregate-
113 specific axons over time, a set of 3.0mm-long, bidirectional "dual-color" micro-TENNs were
114 simultaneously generated such that one aggregate expressed green fluorescent protein (GFP)
115 while the opposing aggregate expressed mCherry (n = 6). Finally, for quantitative validation of
116 the growth model, 2.0mm-long, unidirectional micro-TENNs were transduced to express GFP
117 and generated with approximately 20E^3 neurons per aggregate (n = 6) or 8.0E^3 neurons per
118 aggregate (n = 6) for characterization as described below. Micro-TENNs were imaged under
119 phase contrast microscopy (magnification: 10x) at 1, 3, 5, 8, and 10 days in vitro (DIV) using a
120 Nikon Eclipse Ti-S microscope paired with a QIClick camera and NIS Elements BR 4.13.00
121 (National Instruments). In addition to phase contrast microscopy, the bidirectional dual-color
122 micro-TENNs were imaged at 1, 2, 3, 5, and 7 DIV using a Nikon A1RSI Laser Scanning
123 confocal microscope paired with NIS Elements AR 4.50.00.

124 To quantify micro-TENN growth rates over time, the longest identifiable axons were measured
125 from phase images at each DIV using ImageJ (National Institutes of Health, MD). Lengths were
126 measured from the leading edge of the source aggregate (identified at 1 DIV) to the neurite tip,
127 and growth was measured until axons from the aggregate either spanned the micro-TENN
128 length (unidirectional) or began to grow along axons from the opposing aggregate
129 (bidirectional). Growth rates were averaged at each timepoint to obtain a growth profile for
130 unidirectional micro-TENNs with 20E^3 and 8.0E^3 neurons/aggregate. The peak growth rates for
131 each group were compared using an unpaired t-test, with $p < 0.05$ set as the baseline for
132 statistical significance.

133 To characterize axonal density with respect to cell count, phase images of unidirectional micro-
134 TENNs with either 20E^3 (n = 6) or 8.0E^3 (n = 6) neurons/aggregate at 5 DIV were imported into
135 ImageJ. 10-µm long rectangular regions of interest (ROIs) spanning the inner diameter (final
136 ROI dimensions: 180 µm x 10 µm) were taken at 50% and 75% of the micro-TENN lengths. The
137 axon density at these two locations was quantified as the percentage of the ROI populated by
138 axons. Densities were averaged for the 20E^3 and 8.0E^3 groups and compared at each location
139 via unpaired t-test with $p < 0.05$ as the baseline for significance. All data presented as mean ±
140 s.e.m.

141 To characterize axon distribution, unidirectional micro-TENNs were fabricated and labeled with
142 GFP (n = 5). At 10 DIV, micro-TENNs were gently drawn into a 22-gauge needle and vertically
143 injected into a block of "brain phantom" agarose (0.6% w/v). Micro-TENNs were injected such
144 that the aggregate was ventral with axon tracts projecting downward. Post-injection, micro-
145 TENNs were imaged on a Nikon A1RMP+ multiphoton confocal microscope paired with NIS
146 Elements AR 4.60.00 and a 16x immersion objective. Micro-TENNs were imaged with a 960-nm

4

147 laser, with sequential 1.2μm-thick slices taken along the longitudinal axis (i.e. X-Y projections
148 along the micro-TENN length). Post-imaging, the X-Y projections were used to generate a 3D
149 reconstruction of the micro-TENN; cell bodies, axon bundles, and single axons were then
150 manually identified via co-registration of the X-Y projections and 3D structure.

Computational Model Development

152 The elongation and the growth direction of the neurites in the model is guided by concentration
153 gradients. Each tip of each neuron is a diffusion source in free space. The bifurcation of the
154 neurites is assumed to be a stochastic process, i.e. branching is associated with a time
155 dependent probability function at each node. This framework aims to emulate the growth and
156 bifurcation of micro-TENN neurons, however by using simple diffusion principles, it avoids the
157 underlying biological complexity. All of the tips of the neurite tree are assumed to participate in
158 the extension and branching process. Furthermore, extension and branching of each node are
159 modeled as independent processes. This has computational advantages such as improved
160 speed and ability to parallelize on a large scale.

161 The model uses continuous space/discrete time approach to allow freedom in the outgrowth
162 direction and elongation. Space is bounded by the inner diameter of the hydrogel micro-column.
163 The diameter and length of the tubular hydrogels, 180 μm and 2 mm respectively, are based on
164 experiments previously performed by the Cullen Lab [1], [3]. In the micro-TENNs, axonal
165 extension was measured approximately every two days; as such, the size of the fixed time
166 interval of the model is 1% of this two-day interval (i.e. 28.8 minutes). In each time step, each
167 individual axonal tip may (i) extend, (ii) bifurcate into two daughter branches and (iii) change
168 growth direction. In the present implementation, the model uses fixed time steps with functions
169 built upon the diffusion equation and concentration gradients for extension, turning, and
170 branching. The model is developed with the condition that extension rate and turning direction
171 depend on the concentration gradients at the terminal segment of each axon. The extension
172 rate decreases exponentially to zero value [12] as the neurites stop growing due to the limitation
173 of space and essential biochemical factors [14]. Branching probabilities are growing as a
174 function of the simulation time.

175

Modeling Setup: Diffusion Equation and Concentration Gradient

177 Many stochastic models of neuronal activity are based on the theory of diffusion processes [22].
178 Several models have been developed to describe the growth of single neurons using the theory
179 of one-dimensional stochastic diffusion [23]–[27].

180 In our bidirectional growth model, the tips of the neurons are diffusion sources in free space,
181 assuming a constant isotropic diffusion coefficient. The governing equation is:

182
$$D\nabla^2 C = \frac{dC}{dt},$$
(1)

183 where D is the diffusion coefficient (mm^3/s), C is the concentration (mol/mm^3), and t is time
184 (s). In Cartesian coordinates the partial differential equation becomes:

185
$$D\left(\frac{d^2C}{dX^2} + \frac{d^2C}{dY^2} + \frac{d^2C}{dZ^2}\right) = \frac{dC}{dt}$$
(2)

5

186 with boundary conditions:
187
188 $C|_{x,y,z\to\infty} = 0$ (3)
189
190 $\frac{dC}{dx}|_{x\to\infty} = 0, \quad \frac{dC}{dy}|_{y\to\infty} = 0, \quad \frac{dC}{dz}|_{z\to\infty} = 0$ (4)

191 $\int_{-\infty}^{\infty}\int_{-\infty}^{\infty}\int_{-\infty}^{\infty} C(x,y,z,t)\, dxr\, dy\, dz = M$ (5)

192 M is the initial amount of matter (mol). Without loss of generalization, we can choose $M = 1$ for
193 convenience. The initial condition for a point source (X_0, Y_0, Z_0) inside the shell is:

194 $C(t = 0) = \delta(X - X_0)\delta(Y - Y_0)\delta(Z - Z_0),$ (6)

195 where $\delta(X)$ is Dirac's delta function.

196 Thus, the general solution of the diffusion equation becomes:

197 $C(x,y,z,t) = \left(\frac{1}{(4\pi t D)^{\frac{3}{2}}}\right)\left(e^{-\left(\frac{x^2}{4Dt}+\frac{y^2}{4Dt}+\frac{z^2}{4Dt}\right)}\right)$ (7)

Direction of Neurite Outgrowth

199 The outgrowth of neurites is a complex process that is far from fully understood. In actual
200 biological processes, the outgrowth direction of neurites depends on many intracellular and
201 extracellular cues, which may cause large fluctuations in outgrowth directions [28], [29].

202 Our model is a Markov process: it assumes that the new outgrowth direction depends on the
203 previous outgrowth direction and on the concentration gradients of the growth tips. For each
204 growth tip, the concentration gradients are normalized to preserve the Markovian nature of the
205 model.

206 The outgrowth direction is:

207 $D_2 = D_1 + S_1\nabla C + S_2 E_1,$ (8)

208 where S_1 is the sensitivity to concentration gradients, S_2 is the sensitivity to the direction
209 perturbation, D_1 is the previous direction vector, ∇C is the normalized concentration gradient,
210 and E_1 is the stochastic direction perturbation term.

211 Besides the gradients, a stochastic term E_1 in Equation 8 is introduced to cause small
212 fluctuations in the growth direction. Controlling this term in the simulation allows the control of
213 the magnitude of deviation of the growth direction. Therefore, the component in the axial
214 direction of the cylindrical tube has the largest value, while the components in the radial
215 direction are relatively small.

216

Rate of Neurite Extension

218 The rate of extension of a neurite may vary considerably and is determined both by the external
219 environment and by the internal state of the neurite [30]–[36]. In general, the extension rate
220 decreases gradually with increasing distance from the soma [16]. In our model, the description
221 of neurite extension rate follows the trend of experimental growth rate measured in

6

222 unidirectional micro-TENNs. In each time step, the elongation of a single neurite is represented
223 by the function,

224 $$L = At^2 \left(v_{0_{grad}} \nabla C + v_0 E_2 \right) 2^{-\frac{t}{\tau}}$$ (9)

225 $v_{0_{grad}}$ is the growth rate related to the gradients. v_0 is the base extension rate and E_2 is random
226 process to cause fluctuation in v_0. t is the simulation time, τ controls decreasing speed of the
227 extension rate and A is a scaling factor.

228

229 Growth Tip Position
230 The coordinates at the next step of a growth tip are determined by the coordinates from the
231 previous step, the outgrowth direction, and the extension rate. The new position in each time
232 interval is given by

233 $$P_2 = P_1 + D_2 L$$ (10)

234 where P_1 is the current tip position. However, this tip migration position cannot be accepted until
235 it satisfies the coordinate restrictions of radial constraint and overlap avoidance.

236

237 Branching Probability, Rate of Branching, and Growth Rate After Branching

238 Neurite branching patterns are complex and show a large degree of variation in their shapes .
239 Random branching on the segment indeed results in large and characteristic variations in the
240 structures of the tree. As previous research has highlighted [12], [37], branching is assumed to
241 occur exclusively at terminal nodes. Our model describes branching as a stochastic process.
242 For each time step, for each of the terminal nodes in the growing tree, a branching probability p_j
243 to form two new daughter nodes in a given time interval is assigned.

244 The probability of a branching event at each given terminal node j is given by:

245 $$p_j = \left(1 - e^{-\frac{t-t_{ib}}{\tau_b}} \right) Pb$$ (11)

246 The time-dependent branching probability p_j of a given terminal node j is dependent on several
247 terms: the steady state branching probability Pb ($Pb|_t = \infty$), simulation time t, the branching
248 time step t_{ib}, and a branching time constant τ_b. The equation assumes that the branching
249 probability of terminal nodes per time step remains constant for all tips. Branching probabilities
250 are growing with the total simulation time. Such a function was necessary to match the shape of
251 increasing number of dendritic terminal nodes during outgrowth of the micro-TENNs. The
252 stochastic process of branching is also restricted by another random value E_3; branching could
253 only occur when both p_j and E_3 are greater than a certain value B. The value of B can be
254 determined by the branching probability from experimental data. When a branching event takes
255 place, two daughter terminal nodes are instantaneously added to the end of the existing
256 terminal segment [38], which then becomes an intermediate segment.

257 The growth rate of the generated trees is closely related with segment outgrowth direction and
258 extension. We only consider the extension distance in the axis direction as the growth distance.

7

259 Thus, the growth rate is determined by the difference between the z components of the nodes.
260 In the model, we force the growth cones to extend preferentially in the axis direction and the
261 turning is relatively small. Therefore, the segment extension rate is the strongest factor to
262 determine the growth rate. An estimate of v_0, and τ is obtained from the experimental growth
263 rate. The optimization of the elongation parameters involves a comparison of the experimental
264 and model segment extension rate.
265
266 With the current implementation, the branching probability increases with simulation time. The
267 steady-state branching probability Pb and time constant τ_b are supposed to be extracted from
268 experimental images. By controlling the values the values of Pb and τ_b, we have control over
269 the morphology of the simulated neurites, since Pb controls the branching density and τ_b,
270 controls how early in the process branching begins. In the extreme case of $Pb = 0$, we can
271 generate a morphology with no branching.

272 Radial Constraint
273 Experimentally, micro-TENNs were grown within miniature tubular hydrogels. In the simulation,
274 the outgrowth process is also restricted within the tubular space (in this particular case, 180
275 micrometers in diameter [1], [3]), however the model allows different simulation radii to be
276 employed. At each time step, the radial components of all the terminal nodes are tracked. If a
277 radial component of a given node does not satisfy the tubular constraint, the node will be re-
278 oriented to stick on the tubular wall.

279 Overlap Avoidance
280 The branches and extensions of neighboring neurites often target a shared or adjacent position.
281 All the neurites are competing for space and avoiding overlap. Space competing is achieved by
282 the concentration gradients. Overlapping is avoided by checking the distance from the new
283 position to the surrounding existing segment tips. The model re-orients the growth direction
284 when the extend position is sufficiently close to others.

285 Bundling and Helicity
286 The model accommodates fiber bundling. This is achieved through an attraction term A, i.e. the
287 new position in each time interval becomes:

288 $$D_2 = D_1 + S_1 \nabla C + S_2 E_1 + S_3 A,$$ (12)

289 where S_3 is a sensitivity to attraction (values between zero and one) that controls the bundle
290 formation. In order to construct the attraction term A, we introduce an attraction radius of
291 influence (RI). Every tip that falls within the RI is attracted to the centroids of all the tips that are
292 within the RI. Larger values of RI lead to the formation of fewer bundles and vice versa. Thus,
293 selection of different values of RI allows different morphologies with a different number of
294 bundles. The model naturally provides an additional feature: tips belonging to a given bundle
295 that fall outside of the RI at a given time step can form their own bundle, effectively allowing for
296 a bundle to split. Such an effect is observed experimentally.

297 Helicity is another feature that was introduced to the model aiming to reproduce observed
298 experimental micro-TENN morphologies. Very often, single axons and axonal bundles once
299 reaching the inner wall of the micro-column, form a helix. Our model allows control over both the
300 slope of the helix formed by an axon (or axonal bundle), as well as its helicity (handedness).

301 Parameter Optimization

302 Finding a best fit of the model-generated neuronal morphologies with an experimental data set
303 requires an iterative comparison of experimental and model shape properties. In the search
304 strategy, some parameters in the model are directly related to properties of the experimental
305 data or images. For instance, the parameters $v_{0_{grad}}$, v_0, and τ predict the growth rate in axis
306 direction. The branching process governed by parameters τ_b, P and B fully determine the
307 topological structure of the generated trees. These parameters are directly related to segment
308 branching rate. The time step is selected to be $\Delta t = 0.02$ days. Since v_0 is extracted from the
309 experimental data, the selection of the value of the diffusion coefficient D is guided by the
310 restriction:

311 $$D \leq \frac{1}{2}\frac{L_0^2}{\Delta t},$$ (13)

312 where $L_0 = L(t = 0)$ is the initial extension.

313 Finally, the simulations were carried out on a laptop (Windows 10 Enterprise 64, Intel i7-
314 7700HQ CPU @ 2.80GHz, 2801 Mhz, 4 Cores, 16GB DDR3 RAM). All code with is freely
315 available at: https://github.com/PSUCompBio/GrowthModel.

316 # Results

317 Examples of Micro-TENNs Morphologies

318 Variation of model parameters like sensitivity to attraction S_3 and radius of influence RI allows
319 us to generate different morphologies. S_3 takes continuous values between zero and one, with
320 $S_3 = 0$ corresponding to no bundle formation and $S_3 = 1$ corresponding to tight bundle
321 formation. RI controls the number of bundles formed. **Figures 2, 3** and **4** demonstrate various
322 unidirectional and bidirectional morphologies for different values of RI and S_3 for micro-TENNs
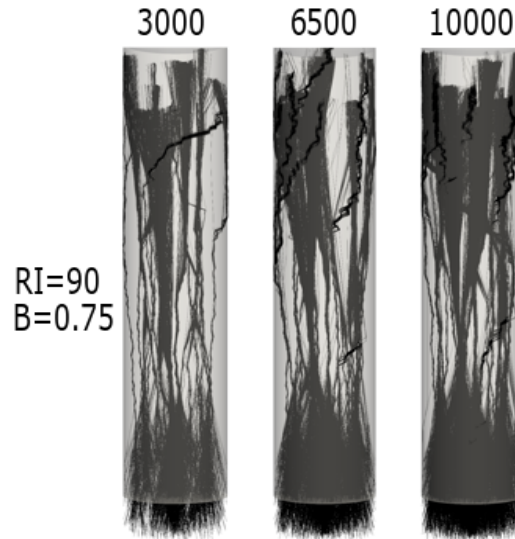323 seeded with 3000, 6500 and 10000 cells.

324
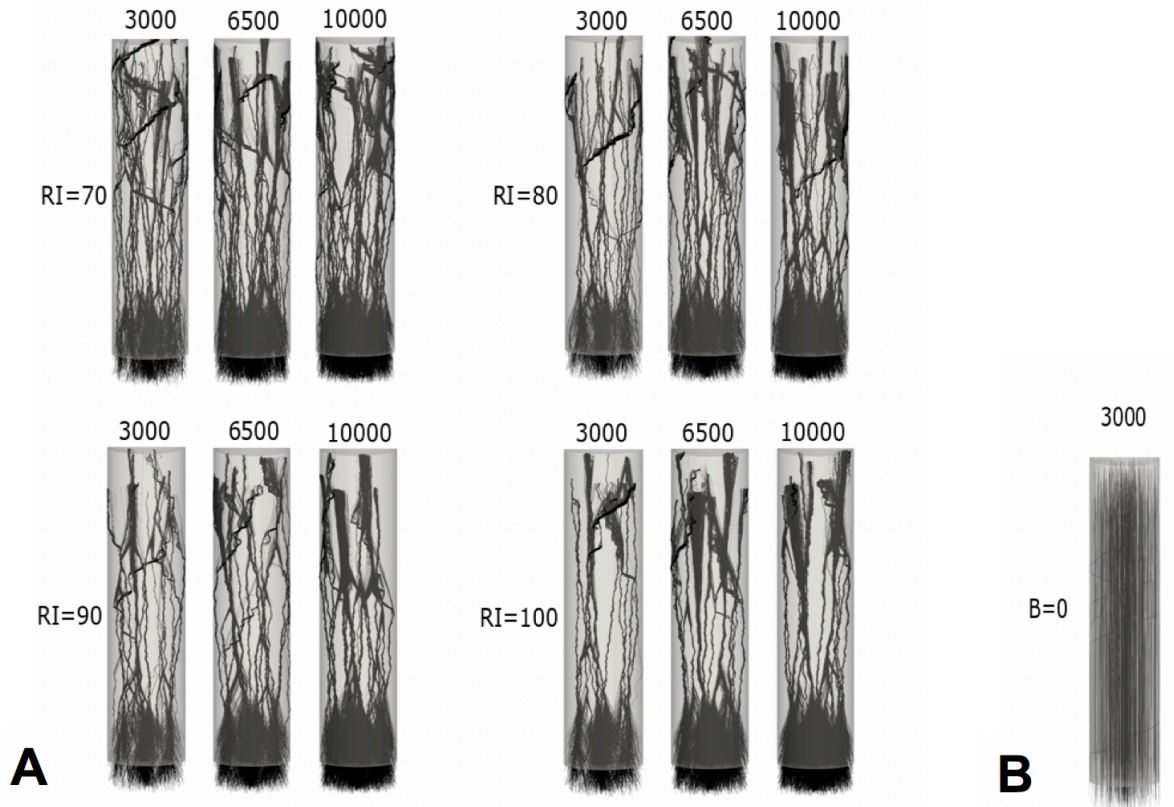
Figure 2. Example of unidirectional model-generated micro-TENN morphologies: (**A**) Twelve morphologies for micro-TENNs of length L=2000 μm and radius R=180 μm, number of seeded cells 3000, 6500 and 10000, and RI=70, 80, 90 and 100 μm, respectively. S_3=1 causes tight bundle formation. (**B**) S_3=0 guarantees no bundle formation.
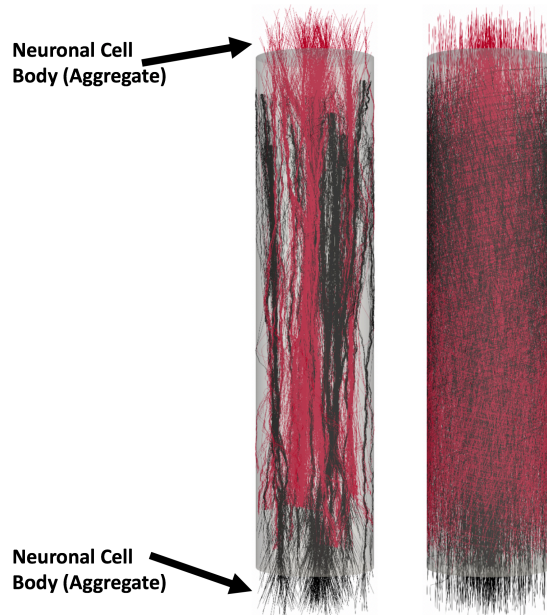
329

330

331

Figure 3. Example of unidirectional model-generated micro-TENNs: Micro-TENNs of length =2000 μm and radius R=180 μm, number of seeded cells 3000, 6500 and 10000, and RI= 90 μm. Here S_3=0.75, bundles are not compact.

332

333

334

335

Figure 4. Example of bidirectional model-generated micro-TENNs: Analogously to the unidirectional case, the model can generate bidirectional morphologies. The micro-TENNs have length L=2000 μm and radius R=180 μm, the number of seeded cells is 3000. Here S_3=1 and RI= 90 μm shows bidirectional axonal bundle formation (left), in the case S_3=0 no bundles are formed (right). Neuronal cell bodies (aggregate) are labeled on each end but are hidden for clarity.

336

11

337 Experimental Validation of Axonal Growth Rate
338 The model simulated the growth processes for unidirectional and bidirectional micro-TENNs
339 when grown to 2000 μm. **Figure 5** shows images of unidirectional micro-TENNs of
340 approximately 8000 and 2000 neurons, as well as measured and computed growth rate. The
341 optimized parameters, $v_0 = 15, v_{0grad} = 0.008$ and E_2 is a random uniform value between 0.8
342 and 1, provided an excellent fit with the experimental data. The result show that extension rate
343 first increases, then decreases slowly with increasing distance from the soma. This is the trend
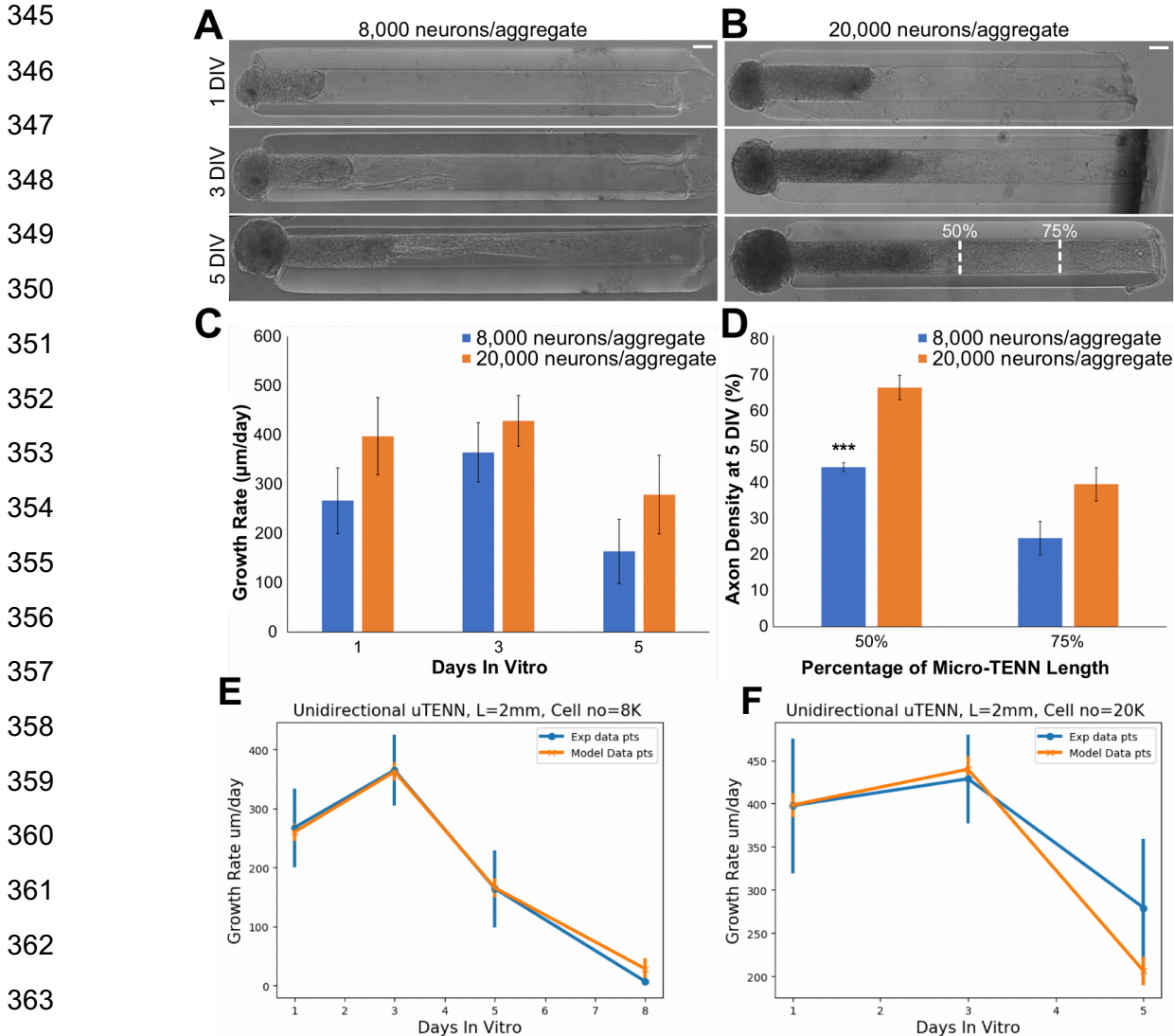344 for both the unidirectional and bidirectional growth rates.

Figure 5. Validation of simulated growth rates *in vitro*. (A) Phase images of a unidirectional micro-TENN with approximately 8,000 neurons at 1, 3, and 5 DIV. (B) Phase images of a unidirectional micro-TENN with approximately 20,000 neurons at 1, 3, and 5 DIV. Both micro-TENN groups exhibited rapid axonal growth over the first few DIV. Scale bars: 100 µm. (C) Growth rates from both micro-TENN groups at 1, 3, and 5 DIV. Micro-TENNs with ~20,000 neurons/aggregate exhibited qualitatively faster growth rates than those with ~8,000 neurons/aggregate, although there were no statistically significant differences in growth rates. (D) Axon density at 5 DIV across the two groups at 50% and 75% along the micro-TENN length (as illustrated in (B)), quantified as the percentage of the microcolumn channel occupied by axons. Micro-TENNs with ~20,000 neurons/aggregate showed higher axon densities than those with ~8,000 neurons/aggregate, although this was only significant at 50% along the micro-TENN length (*** = p < 0.001). (E) Experimental versus model growth rate for unidirectional micro-TENN with 8,000 neurons. (F) Experimental versus model growth rate for unidirectional micro-TENN with 20,000 neurons.

12

369   **Figure 6A** shows a 3D reconstruction of a unidirectional micro-TENN at 10 DIV. Four
370   corresponding slices were extracted for cross-sectional comparison to the computed results.
371   **Figure 6 B-E** show each slice and provide arrows to distinguish between neuronal cell bodies,
372   axon bundles, and single axons. In order to compare morphologies, we use two model
373   generated X-Y projections along the Z-axis (**Figure 7**) that resulted from a micro-TENN
374   simulation (inner radius 180 μm, length of 2mm, the number of seeded cells is 20,000). The
375   model generates realistic morphology with single axons and axon bundles along the inner wall
376   comparable to the experimentally reconstructed morphology in **Figure 7**.
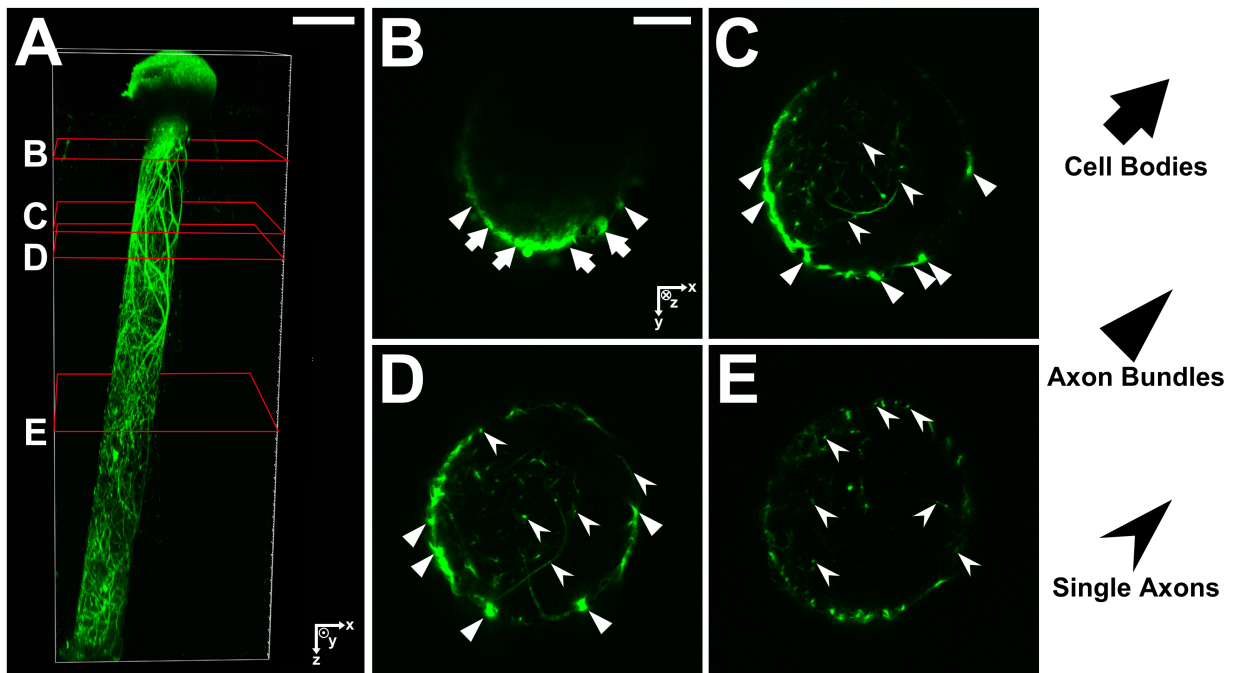
377

Figure 6. **(A)** 3D reconstruction of a unidirectional, GFP-positive micro-TENN at 10 DIV. **(B-E)** X-Y projections of the micro-TENN from (A) at the sections outlined in red. Orientation of the z-axis (positive) is into the page. Neuronal cell bodies (arrows) can be seen near the aggregate region in (B), from which axonal bundles (triangles) project and split into individual axons (caret). Scale bars: 200 μm (A); 50 μm (B).

378

379

380

381

382

383

384

385

386

387

388 **A**   **B**
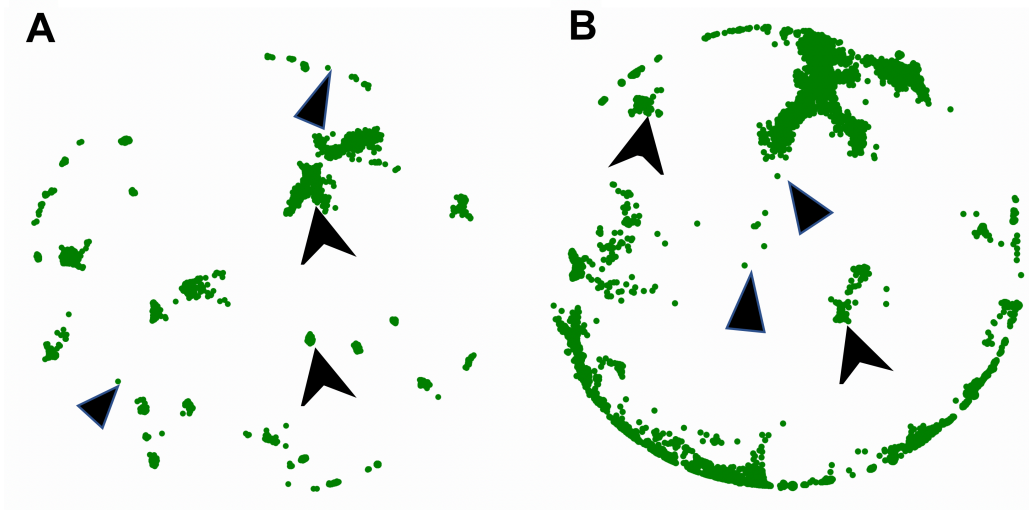
389

390

391

392

393

394

395

396

397

Figure 7. Model generated morphology of a unidirectional micro-TENN with inner diameter of 180 μm, length of 2mm and approximately 20,000 neurons. **(A)** X-Y projection at Z= 910 μm, model **(B)** X-Y projection at Z=1380 μm, model.

398

399 The computational algorithm, employed by our model is scalable as demonstrated on **Figure 8**,
400 which shows the simulation runtime as a function of simulated number of cells (100, 1000 and
401 10000).

402
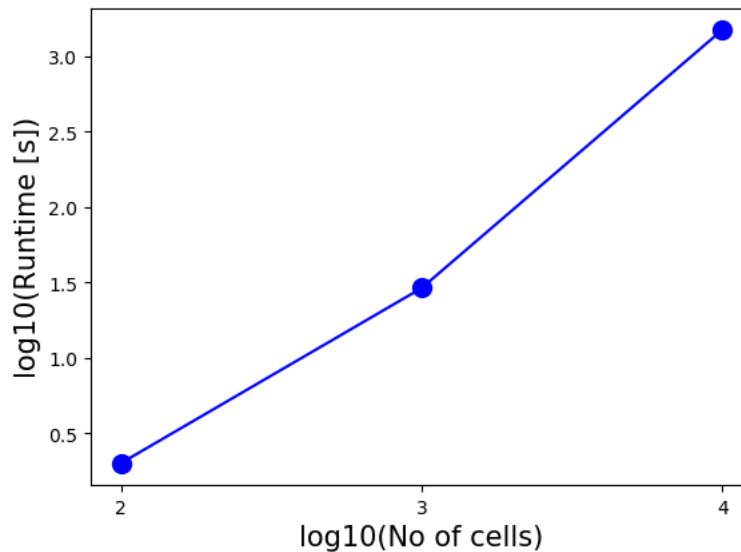
403 **Figure 8. Scaling and computational speed.** Simulations were performed for 100, 1000 and 10000 cells for the
404 unidirectional micro-TENN with diameter 180 μm and length 2mm. The simulation runtime was 1.99 s, 28.93 s and 1500.45 s, respectively.

405

14

Discussion

406

407 As a neural network model, micro-TENNs permit systematic interrogation of different
408 contributors to neuronal growth and development in a three-dimensional, anatomically-relevant
409 environment. Indeed, by providing precise control of the neuronal subtypes within the
410 engineered aggregates, the extracellular matrix and milieu, as well as the potential presence of
411 supporting glial cells, the micro-TENNs provide an ideal platform for the evaluation of interplay
412 between intrinsic and extrinsic mechanisms of neuronal growth and neurite extension. For
413 instance, the 3D biomaterial columnar encasement provides an unprecedented engineered
414 environment to study the multi-faceted and often synergistic contributions of haptotactic
415 [mediated by ECM (e.g., laminin, collagen) and cell-surface ligands (e.g., cadherins, L1)],
416 chemotactic [mediated by growth factor gradients (e.g., nerve growth factor, glial derived
417 neurotrophic factor) that can be attractive or repulsive], and mechanotactic [dictated by
418 substrate geometry (e.g., curvature) and mechanical properties (e.g., stiffness)] on axonal
419 outgrowth and pathfinding [39], [40]. To date, micro-TENNs have been generated with lengths
420 ranging from 1-30 mm, and inner diameters as small as 160µm [4]. Moreover, the introduction of
421 "actuator proteins" such as channelrhodopsin-2 (a light-sensitive ion channel for optically-
422 induced neuronal stimulation) and/or activity markers such as the fluorescent calcium reporter
423 GCaMP also provide a range of techniques to both modulate and monitor neuronal activity
424 within the micro-TENN over time [5]. This controllability makes micro-TENNs an ideal testbed
425 for eliciting and studying different neuronal phenomena under a range of experimental
426 conditions, all within a three-dimensional architecture more similar to the native brain than
427 traditional 2D cultures or randomly organized 3D cultures.

428

429 The existing models have been applied to study neuronal development *in vivo*, generally in the
430 presence of molecular cues and under no specific geometric restrictions. Of note, those
431 conditions differ from the growth conditions of micro-TENNs, in which gradients of external
432 molecular cues are missing, the matrix is not neural tissue, and the growth space is a narrow
433 tubular environment. Moreover, most of the existing models include complex growth
434 mechanisms, leading to large computational cost. To compliment these previous efforts, there is
435 a need for a computationally inexpensive model (due to the large population of neurons) that is
436 capable of capturing the morphology of axonal growth within geometrical restrictions, including
437 such important behaviors as neurite branching and axonal bundle formation/fasciculation.

438

439 Here we present a fast/computationally inexpensive ad-hoc stochastic process-based simulation
440 framework for the generation of large-scale unidirectional and bidirectional neuronal networks
441 with realistic neuronal-axonal morphologies. These simulations faithfully reproduce the shape of
442 micro-TENNs, which are engineered microtissue networks formed by simultaneous axonal
443 outgrowth of many neurons in a constrained (i.e. encapsulated) space.

444 The main advantage of the model is its conceptual simplicity. It is built on basic principles, yet it
445 can generate various complex morphologies observed experimentally. Another major advantage
446 is the computational speed. The solution of the diffusion equation for each tip is explicit and
447 analytic, thus removing the necessity for a numerical solution for the concentration and the
448 concentration gradients. This makes the model fast and computationally cheap, particularly for a
449 large number of growing neurons. Also, each growth tip represents a separate process, allowing
450 for parallelization and additional speed up of computational.

15

451   A limitation to the model is the introduction of parameters that cannot be extracted directly from
452   experimental data. This can be due to the data resolution or simply to an inability of reliably
453   quantifying certain experimental aspects. The parameter space they form has to be scanned for
454   values that allow realistic neuronal morphologies. Another limitation of the model is the lack of
455   chemical cues in the unidirectional case. While the model allows for additional
456   attraction/repulsion and guidance terms to be introduced, employing direct extrapolation from *in*
457   *vivo* growth models would be challenging.

458   The model is designed to capture some basic biological principles of neuronal development and
459   axonal outgrowth *in vitro*: the competition for space and resources between growth tips,
460   formation of bundles, chirality, the dependence of branching probability on the growth time, and
461   the deceleration of the growth rate over time. The growth rate values in our model successfully
462   reproduce the experimental data. Further development of the model could introduce additional
463   guidance and attraction/repulsion molecular cues once such experimental information is
464   available, thereby systematically adding complexity and the ability to capture synergistic and/or
465   competing features of intrinsic and extrinsic growth parameters.

Future Work

467   One major objective of building the Bidirectional Growth Model is to generate simulations of
468   detailed neuron growth patterns to ultimately enable the study of functional connectivity that our
469   research group has begun [41]. The neuronal growth patterns will be used to serve as the input
470   of a spiking model to study the firing patterns within micro-TENNs and, following implantation, at
471   the distal ends of micro-TENNs upon integration with the host brain neurons. In the output of the
472   growth model, the framework can be used to extract detailed connectivity information.
473
474   The neuronal growth patterns provide the information for searching locations of synaptic
475   connections and help to establish the spiking network simulation. In biological neuronal
476   networks, synapses form where tissues are in sufficiently close proximity. According to
477   experimental design, synapses occur close to the aggregate, which are in the 100 μm range
478   from each end. Synaptic connectivity is estimated based on Euclidian distance (proximity
479   criterion of 0.5 μm). **Figures 9A/2B** gives an example of the locations of these synaptic sites.

16

480
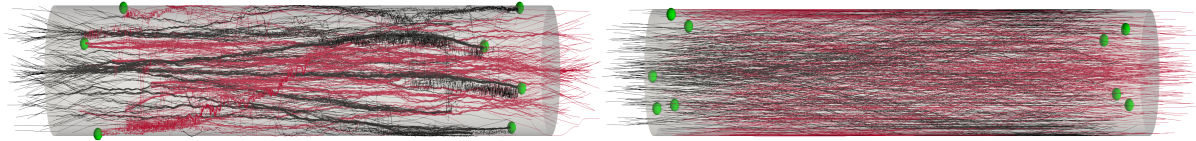
481

Figure 9. Examples of growth pattern and synapses. Illustration of synaptic formation close to the aggregate. The spheres indicate the synapses location. We consider that a synapse is formed when 2 fibers are closer than a threshold distance of 0.5 μm. Synapses occur close to the aggregate (within 100 μm). The connectivity information is extracted for the spiking network simulation. (**A**) The output image of the model: synaptic formation in bidirectional micro-TENNs with axonal bundles. (**B**) The output image of the model: synaptic formation in bidirectional micro-TENNs with no axonal bundles.

482

Conclusion

483

484 The neuronal and axonal growth structures obtained through this model provide a complete
485 growth and connectivity pattern within a custom micro-tissue neural network. The model
486 reproduces both the micro-TENN architecture and the axonal growth rate and distribution. This
487 framework will enable further assessment of structural and functional connectivity, for instance
488 an analysis of synaptic integration that happens close to the aggregate or even outside the
489 micro-column. The extracted information of synaptic connectivity close to the aggregate and the
490 synapse at distal end of micro-TENNs will be the a topic of a future functional connectivity study.
491 We intend to build on this model in order to better understand the spiking network properties of
492 micro-TENNs as so-called "living electrodes" for neuromodulation as well as anatomically-
493 inspired constructs for white matter pathway reconstruction..

Acknowledgements:

494

References

500

501 [1] D. K. Cullen, M. D. Tang-Schomer, L. a. Struzyna, A. R. Patel, V. E. Johnson, J. a. Wolf,
502 and D. H. Smith, "Microtissue Engineered Constructs with Living Axons for Targeted
503 Nervous System Reconstruction," *Tissue Eng. Part A*, vol. 18, p. 120817094501006, 2012.
504 [2] J. P. Harris, L. A. Struzyna, P. L. Murphy, D. O. Adewole, E. Kuo, and D. K. Cullen,
505 "Advanced biomaterial strategies to transplant preformed micro-tissue engineered neural
506 networks into the brain," *J. Neural Eng.*, vol. 13, no. 1, 2016.
507 [3] L. A. Struzyna, J. A. Wolf, C. J. Mietus, D. O. Adewole, H. I. Chen, D. H. Smith, and D. K.
508 Cullen, "Rebuilding Brain Circuitry with Living Micro-Tissue Engineered Neural Networks,"
509 *Tissue Eng. Part A*, vol. 21, no. 21–22, pp. 2744–2756, 2015.
510 [4] L. A. Struzyna, D. O. Adewole, W. J. Gordián-Vélez, M. R. Grovola, J. C. Burrell, K. S.
511 Katiyar, D. Petrov, J. P. Harris, and D. K. Cullen, "Anatomically Inspired Three-dimensional

Micro-tissue Engineered Neural Networks for Nervous System Reconstruction, Modulation, and Modeling," *J. Vis. Exp. JoVE*, no. 123, 2017.

[5] D. O. Adewole, L. A. Struzyna, J. P. Harris, A. D. Nemes, J. C. Burrell, D. Petrov, R. H. Kraft, H. I. Chen, M. D. Serruya, J. A. Wolf, and D. K. Cullen, "Optically-Controlled 'Living Electrodes' with Long-Projecting Axon Tracts for a Synaptic Brain-Machine Interface," *bioRxiv*, Jan. 2018.

[6] L. A. Struzyna, K. D. Browne, Z. D. Brodnik, J. C. Burrell, J. P. Harris, H. I. Chen, J. A. Wolf, K. V. Panzer, J. Lim, J. E. Duda, R. A. España, and D. K. Cullen, "Tissue engineered nigrostriatal pathway for treatment of Parkinson's disease," *J. Tissue Eng. Regen. Med.*, vol. 12, no. 7, pp. 1702–1716.

[7] F. Zubler and R. Douglas, "A Framework for Modeling the Growth and Development of Neurons and Networks," *Front. Comput. Neurosci.*, vol. 3, Nov. 2009.

[8] G. A. Ascoli, J. L. Krichmar, R. Scorcioni, S. J. Nasuto, S. L. Senft, and G. L. Krichmar, "Computer Generation and Quantitative Morphometric Analysis of Virtual Neurons," *Anat. Embryol. (Berl.)*, vol. 204, no. 4, pp. 283–301, Oct. 2001.

[9] P. Hamilton, "A Language to Describe the Growth of Neurites," *Biol. Cybern.*, vol. 68, no. 6, pp. 559–565, Apr. 1993.

[10] B. P. Graham and A. van Ooyen, "Transport Limited Effects in a Model of Dendritic Branching," *J. Theor. Biol.*, vol. 230, no. 3, pp. 421–432, Oct. 2004.

[11] W. Kliemann, "A Stochastic Dynamical Model for the Characterization of the Geometrical Structure of Dendritic Processes," *Bull. Math. Biol.*, vol. 49, no. 2, p. 135, Mar. 1987.

[12] J. Van Pelt, A. E. Dityatev, and H. B. M. Uylings, "Natural Variability in the Number of Dendritic Segments: Model-Based Inferences About Branching During Neurite Outgrowth," *J. Comp. Neurol.*, vol. 387, no. 3, pp. 325–340, Oct. 1997.

[13] A. L. Carriquiry, W. P. Ireland, W. Kliemann, and E. Uemura, "Statistical Evaluation of Dendritic Growth Models," *Bull. Math. Biol.*, vol. 53, no. 4, pp. 579–589, Jul. 1991.

[14] J. A. Villacorta, J. Castro, P. Negredo, and C. Avendaño, "Mathematical Foundations of the Dendritic Growth Models," *J. Math. Biol.*, vol. 55, no. 5–6, pp. 817–859, Nov. 2007.

[15] K.-A. Norton, M. Wininger, G. Bhanot, S. Ganesan, N. Barnard, and T. Shinbrot, "A 2d Mechanistic Model of Breast Ductal Carcinoma in Situ (dcis) Morphology and Progression," *J. Theor. Biol.*, vol. 263, no. 4, pp. 393–406, Apr. 2010.

[16] T. A. HELY, B. GRAHAM, and A. VAN OOYEN, "A Computational Model of Dendrite Elongation and Branching Based on MAP2 Phosphorylation," *J. Theor. Biol.*, vol. 210, no. 3, pp. 375–384, Jun. 2001.

[17] A. Q. Cai, K. A. Landman, and B. D. Hughes, "Modelling Directional Guidance and Motility Regulation in Cell Migration," *Bull. Math. Biol.*, vol. 68, no. 1, p. 25, Jan. 2006.

[18] D. Kiddie, D. McLean, A. Van Ooyen, and B. Graham, "Biologically plausible models of neurite outgrowth," in *Development, Dynamics and Pathology of Neuronal Networks: From Molecules to Functional Circuits*, 1st ed., vol. 147, .

[19] G. J. Goodhill, M. Gu, and J. S. Urbach, "Predicting Axonal Response to Molecular Gradients with a Computational Model of Filopodial Dynamics," *Neural Comput.*, vol. 16, no. 11, pp. 2221–2243, Nov. 2004.

[20] S. Maskery and T. Shinbrot, "Deterministic and Stochastic Elements of Axonal Guidance," *Annu. Rev. Biomed. Eng.*, vol. 7, pp. 187–221, 2005.

[21] A. Stepanyants, J. A. Hirsch, L. M. Martinez, Z. F. Kisvárday, A. S. Ferecskó, and D. B. Chklovskii, "Local Potential Connectivity in Cat Primary Visual Cortex," *Cereb. Cortex*, vol. 18, no. 1, pp. 13–28, Jan. 2008.

[22] P. Lansky and C. Smith, "One-Dimensional Stochastic Diffusion Models of Neuronal Activity and Related First Passage Time Problems," *Trends Biol. Cybemetics*, vol. 1, p. pp.153-162, 1990.

562 [23] S. K. Srinivasan and G. Sampath, "Stochastic Models For Spike Trains Of Single
563 Neurons," in *Springer Science & Business Media*, vol. 16, 2013.
564 [24] H. Tuckwell, *Stochastic Processes in the Neurosciences*. Society for Industrial and Applied
565 Mathematics, 1989.
566 [25] G. L. Yang and T. C. Chen, "On Statistical Methods in Neuronal Spike-Train Analysis,"
567 *Math. Biosci.*, vol. 38, no. 1, pp. 1–34, Jan. 1978.
568 [26] P. I. M. Johannesma, "Diffusion Models for the Stochastic Activity of Neurons," in *Neural*
569 *Networks*, E. R. Caianiello, Ed. Springer Berlin Heidelberg, 1968, pp. 116–144.
570 [27] P. Lánský and V. Lánská, "Diffusion Approximation of the Neuronal Model with Synaptic
571 Reversal Potentials," *Biol. Cybern.*, vol. 56, no. 1, pp. 19–26, Apr. 1987.
572 [28] F. Karube, Y. Kubota, and Y. Kawaguchi, "Axon Branching and Synaptic Bouton
573 Phenotypes in GABAergic Nonpyramidal Cell Subtypes," *J. Neurosci.*, vol. 24, no. 12, pp.
574 2853–2865, Mar. 2004.
575 [29] K. Kalil and E. W. Dent, "Branch Management: Mechanisms of Axon Branching in the
576 Developing Vertebrate Cns," *Nat. Rev. Neurosci.*, vol. 15, no. 1, pp. 7–18, Jan. 2014.
577 [30] J. J. J. Hjorth, J. van Pelt, H. D. Mansvelder, and A. van Ooyen, "Competitive Dynamics
578 during Resource-Driven Neurite Outgrowth," *PLoS ONE*, vol. 9, no. 2, Feb. 2014.
579 [31] G.-H. Li and C.-D. Qin, "A Model for Neurite Growth and Neuronal Morphogenesis," *Math.*
580 *Biosci.*, vol. 132, no. 1, pp. 97–110, Feb. 1996.
581 [32] D. M. Suter and K. E. Miller, "The Emerging Role of Forces in Axonal Elongation," *Prog.*
582 *Neurobiol.*, vol. 94, no. 2, pp. 91–101, Jul. 2011.
583 [33] M. O'Toole, R. Latham, R. M. Baqri, and K. E. Miller, "Modeling Mitochondrial Dynamics
584 During in Vivo Axonal Elongation," *J. Theor. Biol.*, vol. 255, no. 4, pp. 369–377, Dec. 2008.
585 [34] M. P. Van Veen and J. Van Pelt, "Neuritic Growth Rate Described by Modeling Microtubule
586 Dynamics," *Bull. Math. Biol.*, vol. 56, no. 2, pp. 249–273, Mar. 1994.
587 [35] M. O'Toole, P. Lamoureux, and K. E. Miller, "A Physical Model of Axonal Elongation:
588 Force, Viscosity, and Adhesions Govern the Mode of Outgrowth," *Biophys. J.*, vol. 94, no.
589 7, pp. 2610–2620, Apr. 2008.
590 [36] B. P. Graham, K. Lauchlan, and D. R. Mclean, "Dynamics of Outgrowth in a Continuum
591 Model of Neurite Elongation," *J. Comput. Neurosci.*, vol. 20, no. 1, p. 43, Feb. 2006.
592 [37] D. A. Gibson and L. Ma, "Developmental Regulation of Axon Branching in the Vertebrate
593 Nervous System," *Development*, vol. 138, no. 2, pp. 183–195, Jan. 2011.
594 [38] A. van Ooyen, J. van Pelt, and H. Uylings, "Modeling Dendritic Geometry and the
595 Development of Nerve Connections," in *Computational Neuroscience*, CRC Press, 2000.
596 [39] D. K. Cullen, J. A. Wolf, V. N. Vernekar, J. Vukasinovic, and M. C. LaPlaca, "Neural tissue
597 engineering and biohybridized microsystems for neurobiological investigation in vitro (Part
598 1)," *Crit. Rev. Biomed. Eng.*, vol. 39, no. 3, 2011.
599 [40] D. K. Cullen, M. D. Tang-Schomer, L. A. Struzyna, A. R. Patel, V. E. Johnson, J. A. Wolf,
600 and D. H. Smith, "Microtissue engineered constructs with living axons for targeted nervous
601 system reconstruction," *Tissue Eng. Part A*, vol. 18, no. 21–22, pp. 2280–2289, 2012.
602 [41] A. V. Dhobale, D. O. Adewole, A. H. W. Chan, T. Marinov, M. D. Serruya, R. H. Kraft, and
603 D. K. Cullen, "Assessing functional connectivity across 3D tissue engineered axonal tracts
604 using calcium fluorescence imaging," *J. Neural Eng.*, vol. 15, no. 5, p. 056008, Jun. 2018.
605